Surfaces and Interfaces 42 (2023) 103305

Contents lists available at ScienceDirect

Surfaces and Interfaces

journal homepage: www.sciencedirect.com/journal/surfaces-and-interfaces

Formation of laser-induced periodic surface structures on Zr-based bulk metallic glasses with different chemical composition

M. Wolff [a], R. Wonneberger [b], K.E. Freiberg [a], A. Hertwig [c], J. Bonse [c], L. Giebeler [d], A. Koitzsch [d], C. Kunz [d], H. Weber [d], J.K. Hufenbach [d,e], F.A. Müller [a], S. Gräf [a,*]

[a] Friedrich Schiller University of Jena, Otto Schott Institute of Materials Research (OSIM), Löbdergraben 32, D-07743, Jena, Germany
[b] Chemnitz University of Technology, Institute of Materials Science and Engineering, Erfenschlager Straße 73, D-09125, Chemnitz, Germany
[c] Bundesanstalt für Materialforschung und -prüfung (BAM), Unter den Eichen 87, D-12205, Berlin, Germany
[d] Leibniz Institute for Solid State and Materials Research (IFW Dresden), Helmholtzstraße 20, D-01069, Dresden, Germany
[e] Institute of Materials Science, TU Bergakademie Freiberg, Gustav-Zeuner-Straße 5, D-09599, Freiberg, Germany

ARTICLE INFO

Keywords:
Bulk metallic glasses
fs-laser
Laser-induced periodic surface structures
Surface topography
Crystallization
Chemical analysis
Oxidation

ABSTRACT

Bulk metallic glasses (BMG) are amorphous metal alloys known for their unique physical and mechanical properties. In the present study, the formation of femtosecond (fs) laser-induced periodic surface structures (LIPSS) on the Zr-based BMGs $Zr_{46}Cu_{46}Al_8$, $Zr_{61}Cu_{25}Al_{12}Ti_2$, $Zr_{52.5}Cu_{17.9}Al_{10}Ni_{14.6}Ti_5$ (Vit105) and $Zr_{57}Cu_{15.4}Al_{10}Ni_{12.6}Nb_5$ (Vit106) was investigated as a function of their different chemical composition. For this purpose, LIPSS were generated on the sample surfaces in an air environment by fs-laser irradiation ($\lambda = 1025$ nm, $\tau = 300$ fs, $f_{rep} = 100$ kHz). The surface topography was characterized by scanning electron microscopy and atomic force microscopy. Moreover, the impact of LIPSS formation on the structure and chemical surface composition was analyzed before and after fs-laser irradiation by X-ray diffraction and X-ray photoelectron spectroscopy as well as by transmission electron microscopy in combination with energy dispersive X-ray spectroscopy. Despite the different chemical composition of the investigated BMGs, the fs-laser irradiation resulted in almost similar properties of the generated LIPSS patterns. In the case of $Zr_{61}Cu_{25}Al_{12}Ti_2$, Vit105 and Vit106, the surface analysis revealed the preservation of the amorphous state of the materials during fs-laser irradiation. The study demonstrated the presence of a native oxide layer on all pristine BMGs. In addition, fs-laser irradiation results in the formation of laser-induced oxide layers of larger thickness consisting of an amorphous ZrAlCu-oxide. The precise laser-structuring of BMG surfaces on the nanoscale provides a versatile alternative to thermoplastic forming of BMG surfaces and is of particular interest for the engineering of functional material surfaces.

1. Introduction

Bulk metallic glasses (BMGs) are amorphous metal alloys whose disordered atomic structure leads to outstanding physical and mechanical properties. Depending on the alloy system, this implies high hardness and strength, good wear and corrosion resistance, high elasticity and a lower density than typical engineering metallic materials such as stainless steels [1]. BMGs are, therefore, used in the fields of, e.g., micromechanical systems (MEMS), consumer electronics and aerospace industries as well as biomaterials [2,3]. The unique properties of BMGs are particularly related to their chemical composition, which has a significant influence on the thermoplastic formability, mechanical properties, corrosion resistance, glass forming ability and viscosity [4]. A promising material system is represented by Zr-based metallic glasses, which have already been subjected to various laser processing techniques [5–8].

It is already well-known that the functional properties of materials can be adjusted within a wide range by a defined modification of the surface topography. For BMGs, this is typically done via thermoplastic forming [9–11]. However, due to the temperatures required, the metastable amorphous metal tends to crystallize and oxidize during forming [12]. In order to avoid structural changes of the bulk material, ultrashort pulsed lasers with their very short pulse duration in the femtosecond (fs)- to picosecond (ps)-range (i.e., 10^{-15}–10^{-12} s) are a promising tool

* Corresponding author.
E-mail address: Stephan.Graef@uni-jena.de (S. Gräf).

https://doi.org/10.1016/j.surfin.2023.103305
Received 4 May 2023; Received in revised form 23 June 2023; Accepted 17 August 2023
Available online 23 August 2023

for the precise structuring of BMG surfaces on the micro- and nanoscale with reduced heat load during processing [13]. In this context, the generation of laser-induced periodic surface structures (LIPSS) using fs-lasers offers a relatively simple but flexible method to create surface structures on the sub-μm scale. The versatile impact of the periodically modified surface topography on the functional properties has already been demonstrated [14–16]. LIPSS are created by scattering and interference effects within the irradiated focal spot and subsequent selective ablation of the material surface. On metals, typically so-called *low-spatial frequency LIPSS* (LSFL) with spatial periods close to the utilized laser wavelength λ and an orientation perpendicular to the linear laser beam polarization are observed [17,18]. In the following, they are generally referred to as LIPSS here and were the subject of numerous studies on conventional, crystalline metallic alloys [19–21]. In this context, different fs-laser matter interaction processes were investigated including laser-induced oxidation, formation of molten phases and amorphization as well as crystallization at the material surface [22–25]. Although some work already addressed the laser processing of BMGs, the in-depth analysis of laser-induced material modification using suitable characterization methods has received little attention so far [26–29].

In the present study, four Zr-based BMGs of different chemical composition are investigated with regard to their behavior during ultrashort pulsed LIPSS formation. The two commercial alloys $Zr_{52.5}Cu_{17.9}Al_{10}Ni_{14.6}Ti_5$ (Vit105) and $Zr_{57}Cu_{15.4}Al_{10}Ni_{12.6}Nb_5$ (Vit106) are complemented by $Zr_{46}Cu_{46}Al_8$ and $Zr_{61}Cu_{25}Al_{12}Ti_2$, which have been subject to different studies concerning, e.g., the native oxide layer, its atomic structure, and growth rate as well as electrical and tribological surface properties [30,31]. This choice enables a systematic analysis on the influence of the material properties (chemical composition) on fs-laser irradiation including LIPSS formation and ensures the comparability of the results with literature. The LIPSS are produced both in single-spot experiments and – via beam scanning – on large surface areas and subsequently analyzed with regard to their topographical and material-specific properties. One focus is on the characterization of the optical and thermal properties of the BMGs, whose exact knowledge is essential for the laser-matter interaction and, thus, for precise structuring. This also allows to compare the theoretical models with the experimental results concerning material behavior and the formation of specific laser-induced structures. As the second main aspect of this work, the influence of the fs-laser irradiation on the properties and material structure of the differently composed materials is investigated by means of different characterization methods including X-ray diffraction (XRD) and X-ray photoelectron spectroscopy (XPS). The results are related to cross-sectional scanning transmission electron microscopy (STEM) as well as corresponding energy dispersive X-ray spectroscopy (EDXS).

2. Materials and methods

2.1. Sample preparation and characterization

Table 1 shows the nominal chemical composition of the investigated Zr-based BMGs. The alloys were prepared from high-purity elements (≥ 99.99%) by arc melting (Arc Melter, Edmund Bühler GmbH, Germany) in a Ti-gettered high-purity Ar atmosphere. Subsequently, plates with a size of (1 × 10 × 60) mm^3 were produced by centrifugal copper mold casting (HWN Titan 3.3, Linn High Therm GmbH, Germany) and by using an in-situ suction casting device attached to the arc melter, respectively. A detailed description of the fabrication process is described elsewhere [32–34]. Subsequently, the plates were cut into smaller samples with a size of (1 × 10 × 10) mm^3 using a cutting machine (Accutom-50, Struers, USA). Prior to materials characterization and nanostructuring, the sample surface was manually ground and subsequently polished to a mirror-like finish with an average surface roughness $R_a \sim 1$ nm. For this purpose, 180 to 4000 grit SiC abrasive paper and 9 to 1 μm diamond polishing suspension was used in multiple iterative surface preparation steps. During this procedure, it was necessary to grind about 100 μm of the material surface in order to reliably remove crystalline layers due to the manufacturing process [35]. After surface preparation and before laser irradiation, the samples were each ultrasonically cleaned for 10 min in acetone and isopropanol.

Table 1
Nominal chemical composition (at.%) of the investigated Zr-based BMGs.

BMG	Zr	Cu	Al	Ni	Ti	Nb
$Zr_{46}Cu_{46}Al_8$	46	46	8	–	–	–
$Zr_{61}Cu_{25}Al_{12}Ti_2$	61	25	12	–	2	–
Vit105	52.5	17.9	10	14.6	5	–
Vit106	57	15.4	10	12.6	–	5

The optical properties of the BMGs were determined at room temperature by variable angle spectroscopic ellipsometry (M-2000DI, J.A. Woollam Co. Inc., USA) [36]. For this purpose, the ellipsometric angles Ψ and Δ were measured in the wavelength range from 250 to 1700 nm (0.73 - 4.96 eV photon energies) at specific incidence angles between 55° and 75° By means of least-squares-fits of the model to the measured values of Ψ and Δ using B-splines [37], the optical constants (refractive index n, extinction coefficient k) of the metal and the oxide layer thickness t_{OL} were determined for all four BMGs. As the thickness of the native oxide layer is in the nanometer range [38], the optical constants of this material cannot be determined alongside its thickness. Therefore, model assumptions about this layer have to be made. In this case, the oxide was assumed to be pure ZrO_2. As the refractive index n depends on the material structure, the layer was modeled as amorphous zirconia using a model from the database of the ellipsometric software (CompleteEASE, J.A. Woollam Co. Inc., Vers. 6.70). This program was also used to calculate all parameters: the native oxide layer thickness t_{OL}, the spline dielectric function of the metal, as well as the corresponding normal incidence surface reflectivity of the sample surface considering the presence of the native oxide layer.

The thermal behavior of the BMGs was evaluated by thermomechanical analysis (TMA/DMA7e, PerkinElmer, USA) using differential scanning calorimetry and differential thermal analysis. Aluminum crucibles and an inert argon atmosphere were used at constant heating and cooling rates of 20 K/min and 100 K/min, respectively. The measurements were performed with a holding time of 10 min at 313 K prior to both heating processes.

2.2. Laser-based surface structuring

For surface nanostructuring of the polished BMG surfaces, linearly polarized fs-laser radiation (JenLasD2.fs, Jenoptik, Germany) with a central wavelength $\lambda = 1025$ nm, a pulse duration $\tau = 300$ fs, a repetition rate $f_{rep} = 100$ kHz and a maximum laser pulse energy $E_{imp} = 40$ μJ was used. After optical expansion (5x), the fs-laser beam was focused on the sample surface by means of a galvanometer scanner (IntelliScan14, Scanlab, Germany) with integrated f-Theta objective (JENar, Jenoptik, Germany) with a focal length $f_L = 100$ mm.

The interaction between the fs-laser radiation and the different BMGs was first investigated in single-spot experiments for $N = 5$ successive laser pulses according to the method proposed by Liu [39]. Here, the fluence thresholds for LIPSS and melt formation were determined by measuring the squared diameters D^2 of the related surface areas using optical microscopy (VHX-100 K, Keyence, Japan) and plotting them semi-logarithmically as a function of E_{imp}. The Gaussian focal spot diameter $2w_f$ and the respective energy threshold values E_{th} were subsequently determined from the resulting regression line. The obtained Gaussian beam diameter $2w_f = 21$ μm can then be used to calculate the fs-laser peak fluence from the laser pulse energy according to $F_0 = 2E_{imp}/(\pi w_f^2)$.

In order to generate LIPSS on large surface areas, the focused fs-laser beam was scanned in the ambient air atmosphere unidirectionally in x-

direction (i.e., perpendicular to the linear beam polarization) across the metal surfaces using the galvanometer scanner. For this purpose, the scanning speed and the scan line distance were adjusted to $v_x = 0.67$ m/s and $\Delta y = 6$ µm, respectively.

2.3. Characterization of the laser-irradiated surfaces

The laser-irradiated surfaces were characterized with regard to surface morphology and topography by means of scanning electron microscopy (SEM) (EVO40, Carl Zeiss, Germany) and atomic force microscopy (AFM) (JPK Nanowizard 4, Bruker, USA). SEM was performed at an electron acceleration voltage of 20 kV using a secondary electron detector. The AFM was equipped with a silicon tip (PPP-NCHAuD-10, Nanosensors, Switzerland) working at a resonance frequency of 320 kHz in the tapping and QI-mode, respectively. In the context of surface characterization, a focus was set on the regularity and alignment of the fabricated LIPSS, which were quantified by 2D Fast Fourier transform analysis (2D-FFT) of the microscope images with the Gwyddion software (Vers. 2.61) [40]. Corresponding information on the LIPSS modulation depth was obtained from AFM height profiles of the surface topography.

The influence of the fs-laser irradiation on the structure of the different BMGs was analyzed for two different fs-laser peak fluences by X-ray diffraction analysis (XRD) (X'Pert MRD diffractometer, Panalytical, Netherlands) using Co-K_α radiation with a wavelength of $\lambda = 1.7903$ Å and compared with the polished initial surface as reference. For this purpose, the Bragg-Brentano geometry with a rotating sample was chosen, resulting in an X-ray information depth of ≥ 5 µm. In order to identify potential crystallization at the surface of the BMGs, grazing incidence XRD measurements (PW3040/60 X'Pert Pro diffractometer, Philips, Netherlands) were performed. Here, Cu-$K_{\alpha 1}$ radiation with a wavelength of $\lambda = 1.5406$ Å was used to measure the 2θ-range from 5° to 80° with a step size of 0.01° at an incoming beam angle of 2°.

Furthermore, the chemical surface composition was analyzed by X-ray photoelectron spectroscopy (XPS). For this purpose, the sample surfaces were measured before and after fs-laser irradiation, both in overview survey spectra (0 to 1200 eV) and in detailed measurements of the individual elemental transitions with an electron energy resolution of 0.75 eV. The XPS system (PHI 5600, Physical Electronics GmbH, Germany) operated with monochromatic Al-K_α radiation (1486.6 eV photon energy) at an emission angle of 45°. All XPS spectra were calibrated with respect to the main component of C 1 s (284.8 eV) and fitted using Voigt and Gauss functions after Shirley-type background subtraction.

The in-depth composition of the BMGs including, e.g., laser-induced oxide layers was obtained from cross-sections of the laser-irradiated material surface, prepared by lift-out technique using a FEI dual beam focused ion beam (FIB) (Helios NanoLab 600i, FEI/Thermo Fisher Scientific, USA). For this purpose, in a first step, a protective electron beam and ion beam Pt-layer was deposited on the surface and a cross-sectional lamella was prepared in the direction perpendicular to the LIPSS ridge orientation. The voltage was reduced from 30 kV to 5 kV in several steps (four) to reduce the interaction of the Ga-ions with the BMG. During the thinning process, the lamella was tilted between 50.5° and 53.5°. In a second step, the lamella with a thickness of below 100 nm was subsequently investigated by transmission electron microscopy (TEM) (Neoarm 200F, JEOL Ltd., Japan) using an electron acceleration voltage of 200 kV. The TEM is equipped with an aberration corrector for scanning TEM (STEM) together with a wide area (100 mm^2) Centurio EDXS silicon drift detector (JEOL). The acquired EDXS mappings were analyzed with the software package Pathfinder (Vers. 2.6, Thermo Fisher Scientific).

3. Results and discussion

3.1. Material properties of the BMGs

Fig. 1 shows the optical constants n (refractive index) and k (extinction coefficient) of the polished BMGs (solid lines) measured in the wavelength range of 250–1700 nm in comparison to pure Zr (dash-dotted line) as their main component.

The values of n and k are featureless and increase monotonically in the observed spectral range. While small differences can be observed for n among the different compositions, the measured k-values deviate only slightly for the BMGs. At the specific laser wavelength $\lambda = 1025$ nm, refractive indices between 3.11 and 3.42 and extinction coefficients between 4.20 and 4.27 were measured for the investigated materials (Table 2). The reflectivity of all four BMGs including the individual oxide layer thickness is ~ 0.63 at normal incidence almost independent of the chemical composition. Therefore, a similar ablation behavior is to be expected for the BMGs at the utilized fs-laser wavelength. While at $\lambda = 1025$ nm for pure Zr ($n = 4.148$, $k = 3.836$) [41] only a slightly lower reflectance of $R = [(n\text{-}1)^2 + k^2]/[(n+1)^2 + k^2] \sim 0.60$ was calculated, in particular Cu ($n = 0.545$, $k = 6.709$) [42] and Al ($n = 1.317$, $k = 10.022$) [43] both exhibit much larger values of $R \sim 0.95$. These calculations and the ellipsometric measurements confirm that the optical properties of complex alloys cannot be derived from the behavior of the individual constituents [44]. A comparison with the few available studies on the optical properties of metallic glasses [45,46] is difficult, as the material systems investigated are very different and the measurements strongly depend on the sample properties such as surface preparation and material thickness (thin films vs. bulk), etc.

The ellipsometric measurements and the underlying model indicate the presence of a few nm thin native oxide layer. However, the nature

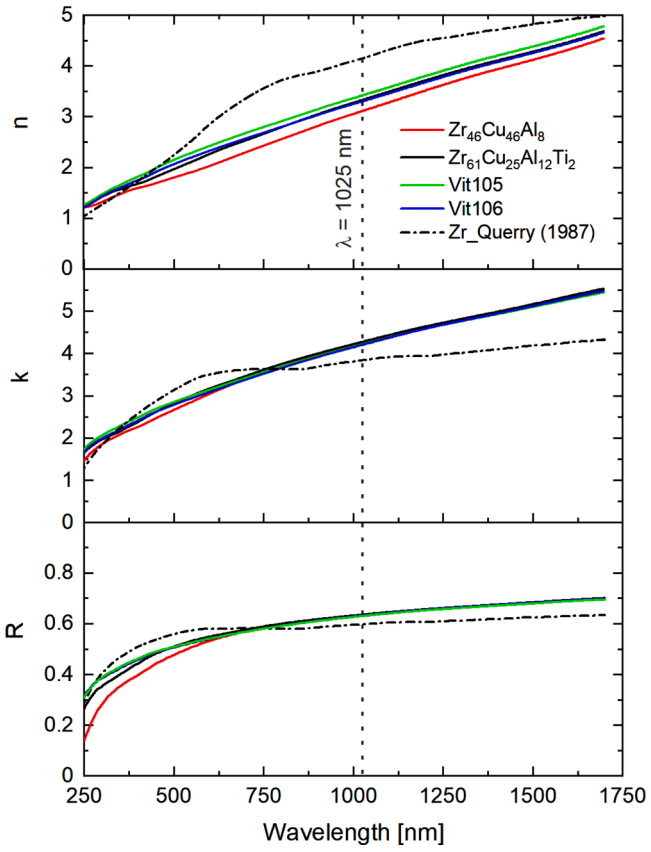

Fig. 1. Refractive index n, extinction coefficient k and reflectivity R at normal incidence determined for the BMGs under investigation compared to pure Zr (values taken from [41]) as a function of illumination wavelength.

Table 2
Optical properties (n: refractive index, k: extinction coefficient, ε: complex dielectric permittivity) of the BMGs at $\lambda = 1025$ nm and reflectivity R at normal incidence derived from ellipsometric measurements under consideration of the determined native oxide layer thickness t_{OL}.

Composition	n	k	Re{ε}	Im{ε}	R	t_{OL} [nm]
$Zr_{61}Cu_{25}Al_{12}Ti_2$	3.33	4.27	−7.15	28.47	0.635	3.6
$Zr_{46}Cu_{46}Al_8$	3.11	4.24	−8.30	26.40	0.634	6.2
Vit105	3.42	4.22	−6.08	28.85	0.629	2.7
Vit106	3.30	4.20	−6.76	27.77	0.632	2.1

and structure of such oxide layers on metallic glasses are not fully understood [30]. It was shown for Zr-based BMG that oxide layers formed on the mechanically ground and on the diamond fine-polished surface are mainly composed of Zr oxide [47]. This agrees well with our ellipsometric analysis where an amorphous ZrO_2 phase is assumed. Regarding the oxide layer thickness t_{OL}, earlier XPS studies on CuAlZr-based BMGs revealed $t_{OL} \sim 3$ nm [38]. In addition, high-resolution TEM-images obtained by Louzguine-Luzgin et al. [30] from $Cu_{47}Zr_{45}Al_8$ (very similar to $Zr_{46}Cu_{46}Al_8$ in the present study) show that crystalline Cu_2O nanoparticles are embedded in an otherwise amorphous oxide layer with a thickness of 10 nm. These values are in the same order of magnitude as t_{OL} determined in the present study. The differences for the individual BMGs, e.g., the relatively small value $t_{OL} \sim 2$ nm for Vit105, might be explained by the type and amount of the individual alloying elements [30].

3.2. LIPSS formation on Zr-based bulk metallic glasses

3.2.1. Single-spot experiments

Fig. 2 shows SEM micrographs of the surfaces after irradiation with $N = 5$ successive pulses at different fs-laser peak fluences. At $F_0 = 0.3$ J/cm^2, the resulting ablation spots are characterized by a regular LIPSS pattern. As is typical for metals, these nanostructures are aligned perpendicular to the linear beam polarization with spatial periods close to the laser wavelength, which is why they can be assigned to low-spatial frequency LIPSS [17]. With increasing F_0, the diameter D of the area covered with LIPSS increases for all BMGs. In addition, an increasing amount of molten and re-solidified material can be observed in the center of the irradiated spot, which is associated with the intense part of the spatially Gaussian beam profile. At $F_0 = 1.1$ J/cm^2, periodic modulations of the surface topography can still be observed in the center of the ablation spot (see e.g. Fig. 2e). They are superimposed to the melt layer with an orientation perpendicular to the LIPSS (i.e. parallel to the linear beam polarization) with spatial periods larger than the laser wavelength. This type of structure can be assigned to so-called grooves, which are created by a spatial energy redistribution due to the interaction between the incident laser radiation with surface waves that might be induced by the LIPSS [48]. Laser peak fluences above $F_0 = 2.8$ J/cm^2 lead to ablation spots where the central surface is very smooth and free of laser-induced structures. The melt layer visible in the center of the ablation spots is characterized by a moderate surface depression, which might result from stronger ablation due to the transiently changing optical properties of the molten phase [49]. Additionally, recoil pressure from laser-induced ablation may transiently act on the underlying residual layer of molten material. To the best of our knowledge, the described behavior has not been reported for crystalline metallic materials and metal alloys so far. This observation indicates an influence of

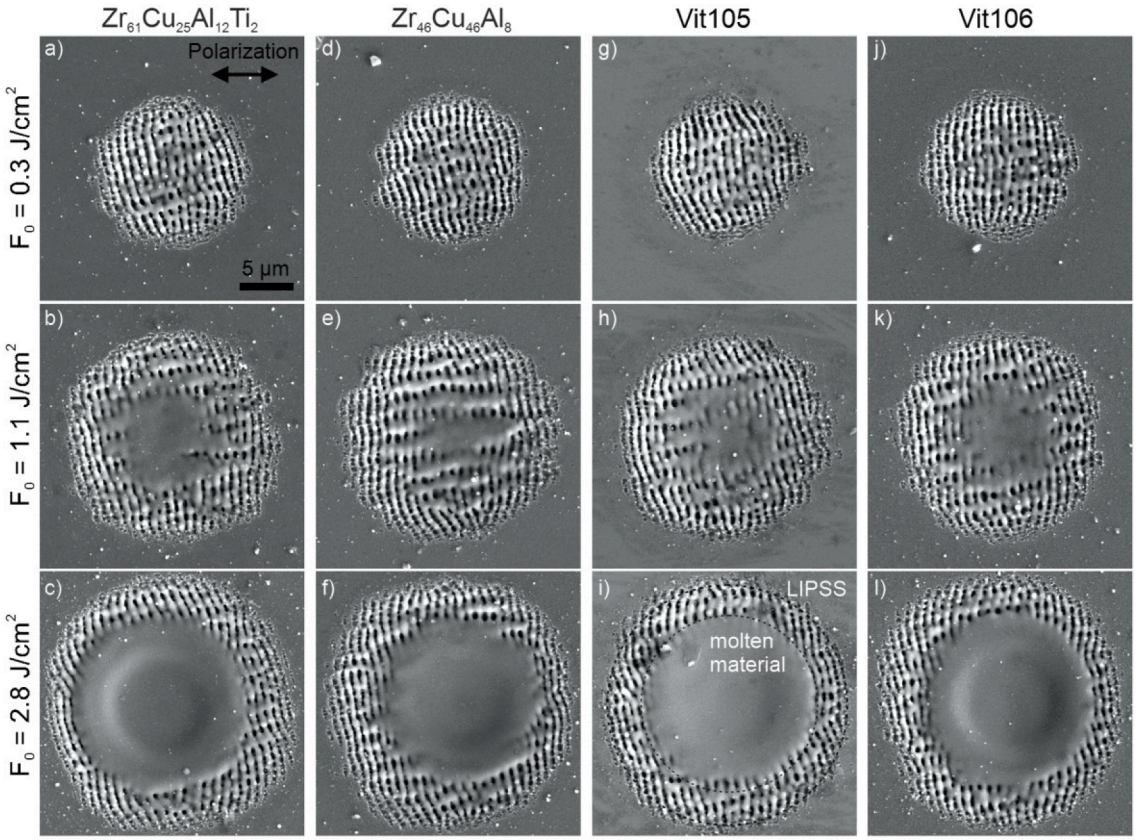

Fig. 2. SEM micrographs of the surface of (a-c) $Zr_{61}Cu_{25}Al_{12}Ti_2$, (d-f) $Zr_{46}Cu_{46}Al_8$, (g-i) Vit105 and (j-l) Vit106 upon irradiation with $N = 5$ successive fs-laser pulses and different laser peak fluence F_0. The direction of linear beam polarization and the scale bar for all ablation spots is indicated in (a). The dotted circles in (i) mark the areas that were evaluated for threshold determination.

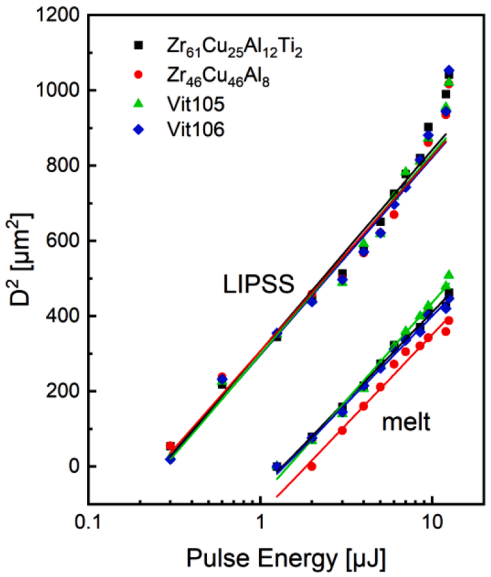

Fig. 3. Evaluation of the formation thresholds of LIPSS and molten material on the different BMGs using $N = 5$ linearly polarized fs-laser pulses and a repetition frequency $f_{rep} = 100$ kHz according to the method proposed by Liu [39].

the amorphous material structure and the associated thermophysical properties. Similar behavior has already been shown for inorganic silicate glasses of different chemical composition [50,51]. Here, the preparation of cross-sections of the single-ablation spots using a focused ion-beam confirmed in particular the absence of LIPSS in the molten area, which could, e.g., simply be covered by a thin layer of melt.

Since the comparison of the ablation spots shows only small visual differences between the BMGs, the formation thresholds of the well-pronounced LIPSS (F_{th}^{LIPSS}) and especially of the molten material (F_{th}^{melt}) were quantified by plotting D^2 in a semilog plot versus E_{imp} as proposed by Liu [39] (Fig. 3). The almost identical slope of the linear regression lines indicates a highly reproducible method, which results in a focal spot diameter of $2w_f = 21$ µm. Extrapolating the linear fit of the measured diameters to zero provides almost equal values of F_{th}^{LIPSS} of the investigated BMGs, which all were found to range from 0.15 to 0.16 J/cm^2. The small deviation of these values derives from the optical constants of the BMGs (Table 2), which suggests an almost identical electromagnetic interaction with the fs-laser radiation. With regard to the melt formation, it is noticeable that $Zr_{46}Cu_{46}Al_8$ has the highest formation threshold compared to the other BMGs. While the threshold values for $Zr_{61}Cu_{25}Al_{12}Ti_2$ (0.78 J/cm^2), Vit105 (0.84 J/cm^2) and Vit106 (0.80 J/cm^2) are at a comparably low level, the value for $Zr_{46}Cu_{46}Al_8$ (1.07 J/cm^2) is significantly increased by a factor of about 1.34. Consequently, the single-spot experiments on $Zr_{46}Cu_{46}Al_8$ under the above-mentioned experimental conditions using comparable fluences are accompanied by the least extent of molten material, which is in good agreement with the SEM micrographs. The different threshold values also correlate with the measured glass transition temperatures T_g, which is highest for $Zr_{46}Cu_{46}Al_8$ ($T_g = 708$ K), when compared to $Zr_{61}Cu_{25}Al_{12}Ti_2$ ($T_g = 673$ K), Vit105 ($T_g = 688$ K), and Vit106 ($T_g = 689$ K) in good agreement with values available in the literature [40]. Therefore, in the case of $Zr_{46}Cu_{46}Al_8$, the expected melt duration (i.e., the time duration for the impact of surface tension gradients and a smoothening of the surface) is shortest during the interaction and LIPSS formation process.

3.2.2. Large-area LIPSS formation on bulk metallic glasses

Fig. 4 shows SEM micrographs of LIPSS fabricated on large surface areas via laser beam scanning with two different fs-laser peak fluences $F_0 = 0.7$ J/cm^2 and 7 J/cm^2, respectively.

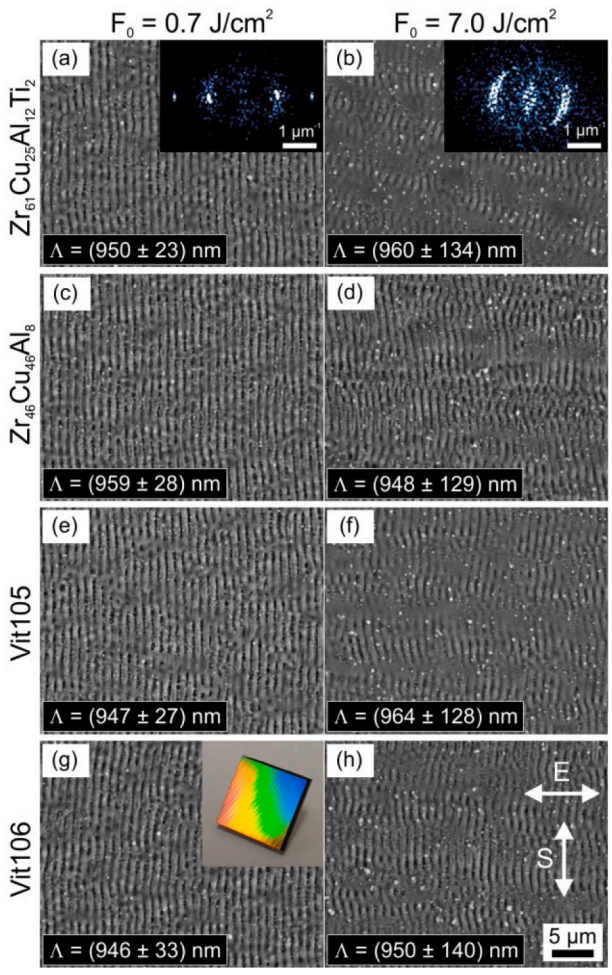

Fig. 4. SEM micrographs of LIPSS fabricated on (a,b) $Zr_{61}Cu_{25}Al_{12}Ti_2$, (c,d) $Zr_{46}Cu_{46}Al_8$, (e,f) Vit105 and (g,h) Vit106 by unidirectional scanning of the focused fs-laser beam across the sample surface using $v_x = 0.67$ m/s and $\Delta y = 6$ µm as well as two different fs-laser peak fluences $F_0 = 0.7$ J/cm^2 (left column) and 7 J/cm^2 (right column). The direction of linear beam polarization (E) and of scanning (S) as well as the joint scale bar for all samples are indicated in (h). The insets in (a) and (b) depict the 2D-FFT spectra calculated from the corresponding SEM micrographs. The inset in (g) uses the example of Vit106 to illustrate the generation of highly-regular LIPSS on large surface areas of (1 × 1) cm^2 through the appearance of structural colors.

These fluence values were chosen on the one hand to minimize the amount of melt detected in the single-spot experiments and thus to obtain the highly regular, well-pronounced LIPSS. On the other hand, the maximum thermal impact of the fs-laser irradiation on the amorphous material structure of the BMGs was to be investigated with the highest possible energy/fluence input at which LIPSS formation still occurs. It should be noted that the threshold values of the single-spot experiments only provide a rough orientation for the utilized pulse number, since the laser beam is scanned over the material surface, resulting in a specific pulse overlap. In order to obtain well-pronounced LIPSS, the parameters $v_x = 0.67$ m/s, $f_{rep} = 100$ kHz and $\Delta y = 6$ µm were used. Considering the determined focal spot radius $w_f = 10.5$ µm, this leads to an effective number of laser pulses per focal spot area $N_{eff\_2D} = (\pi w_f^2 f_{rep})/(v_x \Delta y) = 8.6$ upon laser scanning. This value differs from the single-spot experiments (Fig. 2) because the accumulated fluence is lower in surface processing with a certain (fixed) fs-laser peak fluence when compared to spot processing (e.g. in the intensive center of the Gaussian focal spot). Consequently, an adjustment of the laser and processing parameters is required [52].

For $F_0 = 0.7$ J/cm^2, the processing parameters result in very homogeneous LIPSS patterns aligned exactly perpendicular to the linear beam polarization (indicated in Fig. 4h). The comparison between the different BMGs reveals no significant differences. The corresponding SEM micrographs are all characterized by certain regions at the surface with melted and resolidified material. Apart from a few nanoparticles superimposed on the LIPSS, the patterns show almost no inhomogeneities such as bifurcations or interruptions. The most frequent spatial period Λ calculated by 2D-FFT (see insets in Fig. 4) varies only in a very narrow range of values between 946 and 959 nm (i.e., 0.92 - 0.94λ). From AFM surface topographic height profiles, a modulation depth of the uniform LIPSS patterns between 160 and 210 nm was determined for the investigated BMGs. The large-scale character of the LIPSS patterns and their regularity is further illustrated by the structural colors shown in the inset of Fig. 4g, which appear on a sample size of (1 × 1) cm^2.

Based on LIPSS formation considering the excitation of Surface Plasmon Polaritons (SPPs), the spatial period Λ_{SPP} can be theoretically calculated according to $\Lambda_{SPP} = 2\pi/Re\{\beta\}$ with $\beta = \omega/c \cdot [(\varepsilon_{air} \cdot \varepsilon_m)/(\varepsilon_{air}+\varepsilon_m)]^{1/2}$. Here, ω is the laser angular frequency, c is the speed of light, ε_m is the complex dielectric permittivity of the metal and the dielectric permittivity of the surrounding air atmosphere ε_{air} equals to 1. Using the determined optical constants (Table 2), this calculation results in very similar Λ_{SPP} values for all BMGs in the range between 1020 and 1023 nm at $\lambda = 1025$ nm wavelength. These theoretical values are ~7% larger than the experimentally observed periods. The difference is mainly related to inter-pulse feedback effects [14,17], which reduce the SPP resonance absorption wavelength once the LIPSS-related surface grating deepens [53]. As a consequence, for LSFL on semiconductors and metals, Λ reduces with increasing number of (effective) pulses per spot [52,54].

The high LIPSS regularity obtained at the moderate fluence is illustrated by the 2D-FFT spectrum shown exemplarily for $Zr_{61}Cu_{25}Al_{12}Ti_2$ in Fig. 4a. The two very sharp peaks correspond to a small variation of the determined LIPSS periods. The uniform alignment is quantified by the very small dispersion of the corresponding LIPSS orientation angle (DLOA). According to the study of Gnilitskyi et al. [55], the formation of highly regular LIPSS on large surface areas is usually limited to those metals that are characterized by a high optical damping of laser-driven SPPs. The latter manifests particularly for materials with a large imaginary part of the dielectric permittivity ε when compared to the absolute value of the real part. Consequently, such materials exhibit a small SPP decay length $L_{SPP} = 1/\mathrm{Im}\{\beta\}$ at the corresponding laser wavelength λ. With the ε-values from Table 2, the investigated BMGs reveal values of $L_{SPP} \sim 4.6$ - 5.4 μm very similar to the L_{SPP} of stainless steel, titanium and molybdenum, on which highly regular LIPSS have already been demonstrated experimentally [21,55].

Examination of the SEM micrographs obtained from irradiation with $F_0 = 7.0$ J/cm^2 reveals that both, the fraction of melted and re-solidified areas and the amount of nanoparticles on the surface, have increased significantly. The spatial periods of the partially still visible, well-pronounced LIPSS are comparable to the values determined for $F_0 = 0.7$ J/cm^2, indicating a weak fluence dependence $\Lambda(F)$ here. This may arise from the utilized scan processing approach, where within a scanned line (x-direction) the low intensity wing of the Gaussian beam can "overwrite" the regions (that were previously ablated with the high fluence part of the beam) with LIPSS [52]. In the perpendicular (y-) direction, the surface of the molten areas in between the LIPSS appears rather smooth and little modulated concerning the topography. As a result, the high fluence processed LIPSS patterns exhibit numerous bifurcations and interruptions, which results in a remarkably lower regularity of the entire structured surfaces. This is indicated by the larger variation range of the LIPSS periods evaluated by 2D-FFT, which is increased by a factor of 4 – 5 when compared to the low fluence processed LIPSS. Moreover, the 2D-FFT spectrum for $Zr_{61}Cu_{25}Al_{12}Ti_2$ in Fig. 4b also shows a much broader peak, which is additionally characterized by a significantly larger DLOA. We did not observe any indications of heat accumulation at the utilized pulse repetition frequency of $f_{rep} = 100$ kHz since the nanoscale roughness in terms of LIPSS and superimposed nanoparticles are preserved for both fluences.

3.3. Characterization of laser irradiated bulk metallic glass surfaces

3.3.1. Investigation of the crystallographic structure

Fig. 5 shows the X-ray diffraction patterns of the different BMGs scan-processed with LIPSS at two fs-laser peak fluences $F_0 = 0.7$ J/cm^2 and 7.0 J/cm^2, respectively. The non-irradiated, polished samples as reference are characterized by two broad amorphous maxima at $2\theta \sim 43^\circ$ - 46° and $2\theta \sim 77^\circ$ - 79° These broad peaks or halos are typical for metallic glasses and result from the amorphous state with short-range but no three-dimensional long-range order. Since no discrete peaks can be observed in the X-ray diffraction patterns, a certain degree of crystallization of the reference samples is excluded within the XRD information depth. Considering the utilized X-ray radiation wavelength and the Bragg condition, the 2θ-range determined for the intensity maxima agrees well with literature values available for Vit105 [35,56]. Moreover, the comparison with literature confirms in particular the experimental observation that the position of the halos of the Zr-based BMGs is almost independent of their chemical composition.

After LIPSS formation, the X-ray diffraction patterns of $Zr_{61}Cu_{25}Al_{12}Ti_2$ (Fig. 5a), Vit105 (Fig. 5c) and Vit106 (Fig. 5d) remain unaffected by the fs-laser irradiation at both fluence values. Only a slight shift of the halo positions towards smaller 2θ-angles can be observed with an increasing fs-laser peak fluence. For $Zr_{46}Cu_{46}Al_8$ (Fig. 5b), however, specific reflections appear after laser irradiation even at the low peak fluence of $F_0 = 0.7$ J/cm^2. These can be assigned to different crystalline intermetallic phases that are thermodynamically possible to form in this system [57]. With increasing F_0, the reflections protrude more strongly from the amorphous background in Fig. 5b, which indicates an increasing crystallization. In the case of the higher fluence, a larger residual thermal heat is deposited at the surface, which can affect the cooling rates and may promote crystallization of the amorphous phase. In this context, a key aspect is given by the glass forming ability of the alloys as LIPSS formation is generally associated with selective ablation, i.e., the material surface locally exceeds the vaporization temperature. The resulting temperature gradients lead to the formation of a melt, which was confirmed both in the single-spot experiments (Fig. 2) and during scan processing (Fig. 4). Consequently, the material is subject to a transition between room and vaporization temperature. Nevertheless, the utilized fs-laser pulses provide very fast heating and cooling rates, which, in combination with the low melt layer thickness, lead to an amorphous solidification for $Zr_{61}Cu_{25}Al_{12}Ti_2$, Vit105 and Vit106 as well as only to a moderate crystallization of the amorphous phase for $Zr_{46}Cu_{46}Al_8$.

Nevertheless, the signals from crystalline sub-surface regions might be too small to be detected at the relatively large information depth available for measurements in the Bragg-Brentano geometry. Therefore, surface-sensitive grazing incidence X-ray diffraction was performed for $Zr_{61}Cu_{25}Al_{12}Ti_2$ (Fig. 6a) and Vit105 (Fig. 6b). Vit106 is assumed to behave similarly to Vit105 due to its very similar chemical composition and identical sample preparation. The X-ray diffraction patterns of the two investigated BMGs reveal no reflections – even not at high fs-laser peak fluences. Therefore, the amorphous state of the initially polished sample is still present after fs-laser structuring. For the direct comparison of the reflection positions of both measurements, the different wavelengths of the utilized X-Ray radiation need to be considered.

The strong tendency of crystallization detected for $Zr_{46}Cu_{46}Al_8$ reflects the relatively low glass forming ability of this ternary alloy system compared to the other BMGs [2,58,59]. It is in line with the large value of the glass transition temperature T_g as well as the larger fluence threshold of melt formation, which were both evaluated experimentally for $Zr_{46}Cu_{46}Al_8$.

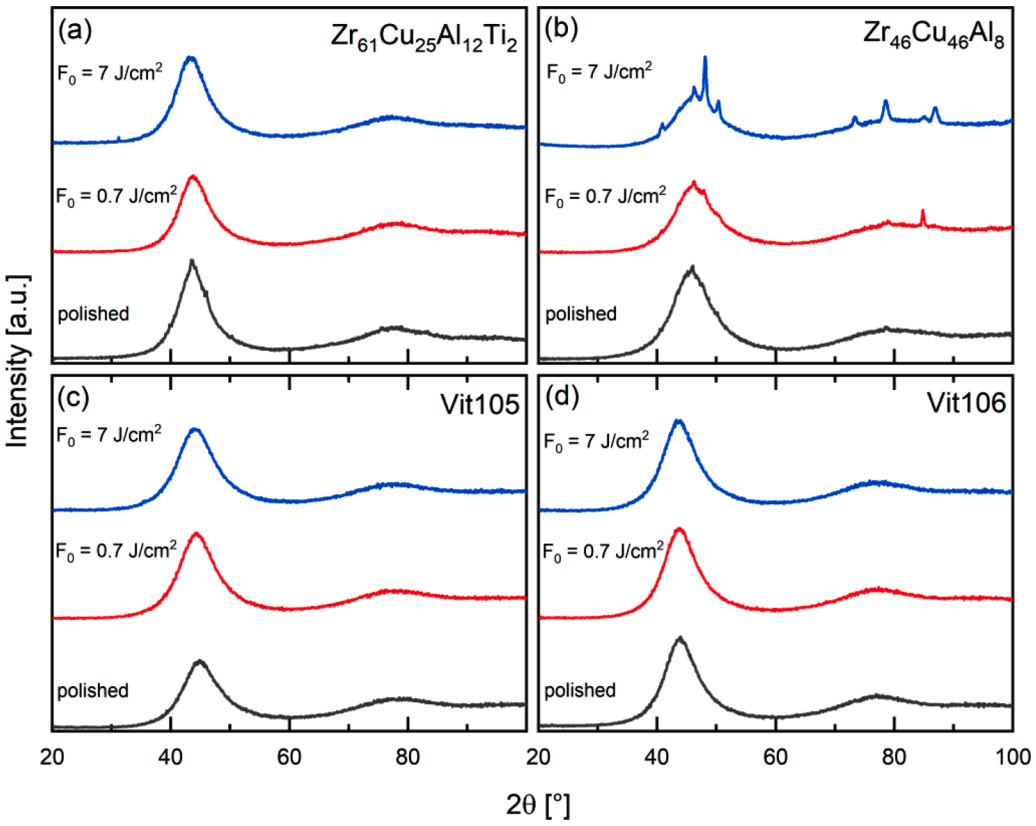

Fig. 5. X-ray diffraction patterns of (a) $Zr_{61}Cu_{25}Al_{12}Ti_2$, (b) $Zr_{46}Cu_{46}Al_8$, (c) Vit105 and (d) Vit106 measured with Co-K_α radiation after irradiation with two different fs-laser peak fluences ($F_0 = 0.7$ J/cm^2 and 7.0 J/cm^2, both for $v_x = 0.67$ m/s and $\Delta y = 6$ μm) compared to the polished, non-irradiated surface as reference. For better visualization, the diffraction curves were shifted and stacked vertically.

3.3.2. Analysis of the chemical surface composition

The chemical surface composition of the samples was analyzed by XPS before fs-laser irradiation and compared to surfaces structured with LIPSS at $F_0 = 0.7$ J/cm^2 and 7.0 J/cm^2, respectively. XPS is especially suitable for destruction free investigation of the uppermost surface region with an information depth of ~7 nm. Fig. 7 presents XPS signals of Zr 3d, Al 2s and Cu 3s as well as O 1s and C 1s core levels. It should be noted that the latter two elements are not intrinsic to the BMGs but unavoidably present at surfaces exposed to ambient atmosphere. Before the detailed discussion of the high-resolution spectra, some aspects of the surface composition are commented. They were derived from total XPS intensity ratios between Zr, Al and Cu considering proper sensitivity factors for the given experimental environment. The results reveal that the surface composition of the untreated polished sample is dominated by Zr. After fs-laser irradiation, the surface composition undergoes remarkable changes. In particular, the Zr concentration decreases strongly, while a significant increase is detected for the amount of Cu. These results underline the fundamental impact of LIPSS formation on the surface characteristics.

The Zr 3d signal in Fig. 7a consists of a doublet situated at binding energies of $E_B = 182.2$ eV and 184.6 eV, respectively. This doublet is a consequence of spin-orbit splitting of the 3d level in $3d_{5/2}$ and $3d_{3/2}$ lines. The energy position agrees with literature values for ZrO_2 [60]. Together with the predominant Zr concentration at the surface, the assumption of a Zr-rich native oxide layer seems to be appropriate for modeling the ellipsometry data above. The low energy region of the upper panel of Fig. 7a reveals a very weak second doublet at $E_B = 178$ eV corresponding to Zr(0). This constellation is typical for Zr-based BMGs. As shown by Heinrich et al. [61], a shift of the Zr doublet to smaller binding energies occurs with increasing material depth, which corresponds to a transition from oxygen-bound Zr at the material surface to metallic Zr in the bulk. With increasing fluence, the line shape broadens. At $F_0 = 7$ J/cm^2, a clear minimum can no longer be observed between the spin-orbit components.

Fig. 7b shows the overlapping Al 2s and Cu 3s core levels. This overlap complicates the analysis but still the components are more clearly separated than in the Al 2p/Cu 3p spectra. Comparing the polished sample in the uppermost panel with the fs-laser irradiated surfaces, the large increase of the Cu concentration on the scale of the XPS information depth becomes immediately evident. The energy position of the Al 2s line ($E_B = 118.8$ eV) fits to Al_2O_3 [60]. It has been proposed that Al acts as oxygen scavenger in the alloy [61]. Indeed, no clear Al(0) signal is present at the low energy side of the spectra indicating predominant Al in its oxidic state within the XPS information depth.

The Cu 3s peak consists of two components at E_B ~ 122.5 eV and ~124.5 eV, which can be assigned to Cu(0) and Cu^{2+} [60]. Their mutual dependence is more evident in the Cu $2p_{3/2}$ spectra (not shown). The initial polished sample is dominated by Cu(0), while for $F_0 = 0.7$ J/cm^2 the relative intensity of Cu^{2+} in form of Cu-oxide and/or hydroxide clearly increases. Compared to the native oxide layer, which is dominated by the Zr-rich oxide, the fs-laser irradiation leads to a modified chemical composition. The latter is particularly characterized by the increased Cu content, which was verified by additional AES measurements (now shown). The exact formation mechanism of this laser-induced oxide layer requires further investigation for a detailed explanation. However, the findings emphasize the complex, highly dynamic processes that occur at the surface during ablation and oxidation, given the extremely fast heating and cooling cycles in an air environment [25].

These observations are also consistent with the behavior of the O 1s line (Fig. 7c). The initial polished sample features a double peak structure, which can be assigned to metal oxide formation and metal carbonates. Another weak component at the high energy side corresponds to hydroxides. After fs- irradiation, the intensity of the low energy peak

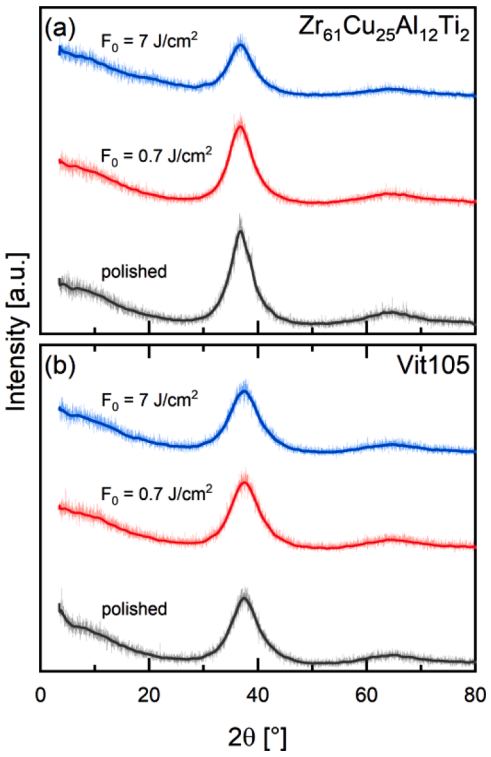

Fig. 6. Grazing incidence X-ray diffraction patterns of (a) $Zr_{61}Cu_{25}Al_{12}Ti_2$ and (b) Vit105 measured with Cu-K_α radiation and an incoming beam angle of 2° after irradiation with different fs-laser peak fluences compared to the polished, non-irradiated surface as reference. The same samples as for Fig. 5 were used. For better visualization, the diffraction curves were shifted and stacked vertically.

(metal oxide) is strongly reduced, while the hydroxide component increases. The observations suggest that the intense low energy peak of the non-irradiated polished sample originates from Zr oxide and the increased high energy component obtained for $F_0 = 0.7$ J/cm^2 results from Cu hydroxide. After LIPSS formation with $F_0 = 7$ J/cm^2, the line shape becomes again broad and featureless.

The C 1s signal in Fig. 7d indicates the presence of adventitious carbon at the surface in terms of C—C single bonds, C—O bonds of organic components and C═O/COOH species originating from adsorption from the surrounding atmosphere during sample storage. Regarding absolute concentration, the fs-laser irradiated samples reveal a larger surface carbon content with respect to the initial polished sample. This higher concentration might be explained by the increased effective surface area of LIPSS offering more capacity for adsorbates per surface unit. The surface contamination with carbon, especially after LIPSS formation, is well-known for stainless steel and other crystalline alloys [24] and is a key aspect in the context of the time-dependent wetting behavior known as “aging effect” [62–64].

Regarding the thickness of the oxide layer, the Zr(0) component detected for the initial polished sample (Fig. 7a) is associated with bulk Zr located below the Zr-rich surface oxide [61]. Its very low intensity indicates an oxide layer thickness of the order of the XPS information depth. Consequently, the absence of any Zr(0) signal for the fs-laser irradiated samples indicates a larger oxide layer thickness compared to the initial polished sample. However, it should be noted that the fs-laser irradiation also leads to a broadening of the spectra, which is why a residual Zr(0) signal could smear out and be indistinguishable from the background.

The XPS spectra of the other three BMGs ($Zr_{46}Cu_{46}Al_8$, Vit105, Vit106; data not shown here) exhibit no significant differences when compared to $Zr_{61}Cu_{25}Al_{12}Ti_2$, both in the polished initial state and after LIPSS processing upon fs-laser irradiation.

To shed more light on the laser-induced oxide layer on the quaternary system $Zr_{61}Cu_{25}Al_{12}Ti_2$, its thickness and composition was investigated in more detail by means of TEM and STEM EDXS analysis of a

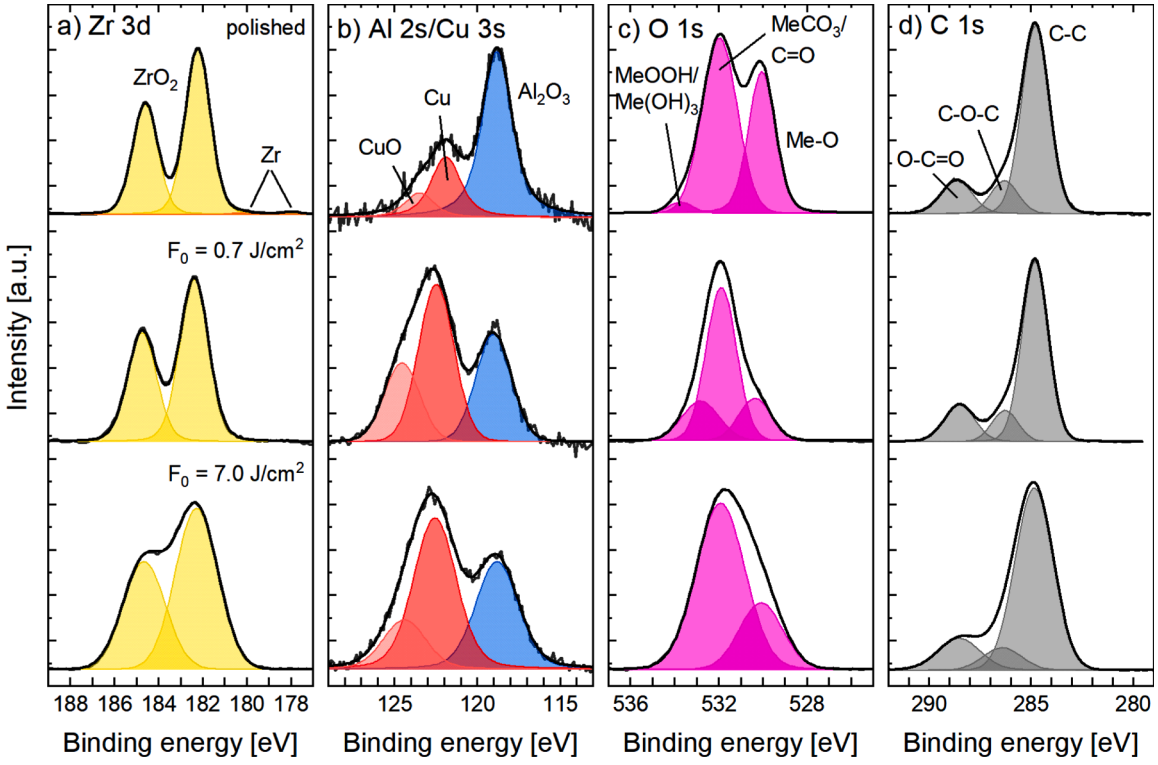

Fig. 7. High-resolution XPS spectra of the surface of $Zr_{61}Cu_{25}Al_{12}Ti_2$ before (polished) and after fs-laser irradiation at $F_0 = 0.7$ J/cm^2 and 7.0 J/cm^2 ($v_x = 0.67$ m/s, $\Delta y = 6$ μm), respectively: (a) Zr 3d peaks, (b) Al 2s/Cu 3s peaks, (c) O 1s peaks, and (d) C 1s peaks.

cross-sectional lamella prepared from the surface irradiated at $F_0 = 0.7$ J/cm^2 (i.e., the surface contains highly regular LIPSS, see Fig. 4, left column). The present study focuses on the state after fs-laser irradiation, since investigations of the native oxide layer by means of high-resolution TEM, EDXS and XPS were already published for the same and for very similar chemical compositions, respectively [30,31,65]. Fig. 8a shows EDXS maps of the individual elements oxygen (O), aluminum (Al), titanium (Ti), copper (Cu), zirconium (Zr), and platinum (Pt), all acquired in the transition region from the bulk of the metallic glass through the oxide layer into the deposited Pt-layer. The corresponding EDXS line scan presented in Fig. 8b was accumulated from the yellow frame along the white line in Fig. 8a. The concentration profiles exhibit a slight deviation from the expected composition of $Zr_{61}Cu_{25}Al_{12}Ti_2$ in the bulk material, which is attributed to the measured oxygen content of about 10 at.%. This relatively large amount can be explained by surface oxidation of the lamella at its front and rear side after focused ion beam preparation and the transfer to the TEM. Since the analysis of the element concentration of the oxide layer also considers the oxygen content, the relative amount of the other elements involved is reduced accordingly.

It becomes evident from the EDXS mappings as well as from the concentration profiles that the laser-induced oxide layer is formed by Zr, Al and Cu. According to the phase diagram, a solubility of ZrO_2 in Al_2O_3 is possible in the equilibrium state [66]. In addition to the XPS measurements, the TEM results show that Cu is detected in both the bulk and the oxide layer. This observation is confirmed by the multilayer distribution of Cu within the EDXS map and the concentration profile of Cu in Fig. 8b, which exhibits two pronounced concentration maxima. A comparable distribution was determined by Sawyer et al. [67] for Vitreloy1b, i.e., a Zr-based BMG with lower Cu content ($Zr_{44}Ti_{11}Cu_{10}Ni_{11}Be_{25}$) than our $Zr_{61}Cu_{25}Al_{12}Ti_2$, using XPS and glow-discharge optical emission spectroscopy. From the perspective of thermodynamics, the oxygen affinity of Al and Zr is higher than that of Cu, as indicated by the gain in free energy (ΔG_f^0) for the formation of Al_2O_3 and ZrO_2 in comparison to CuO [68]. Consequently, the enrichment of Cu in the bulk is presumably the result of the diffusion of Al and Zr from the bulk to the surface. On the contrary, Cu detected directly at the surface indicates the incorporation of oxidic Cu species at the beginning of the laser-induced oxidation process. The enrichment of Cu in the alloy corresponds to the dark seam within the TEM micrograph in Fig. 8a directly at the interface between bulk and oxide layer (marked by the red arrow). According to the FWHM condition, the EDXS concentration profile leads to an oxide layer thickness of ~10 nm, which might be slightly over-interpreted by the selected width of the line scan, the slightly curved interface and blurring due to defocusing and drift during the EDXS measurement. This is confirmed by the high-resolution TEM micrograph of the same area as the EDXS measurement was performed (Fig. 8c), from which a smaller thickness of ~6 nm can be determined for the laser-induced oxide layer. This is almost twice the native oxide layer thickness of the polished $Zr_{61}Cu_{25}Al_{12}Ti_2$ surface (t_{OL} ~ 3.6 nm) obtained from the ellipsometric measurements (see Table 2). The high-resolution TEM micrograph also confirms that the surface oxide layer and adjacent $Zr_{61}Cu_{25}Al_{12}Ti_2$ bulk material is amorphous after fs-laser irradiation at $F_0 = 0.7$ J/cm^2, while the visible regular network planes confirm a polycrystalline grain structure of the surface protecting Pt-cover layer.

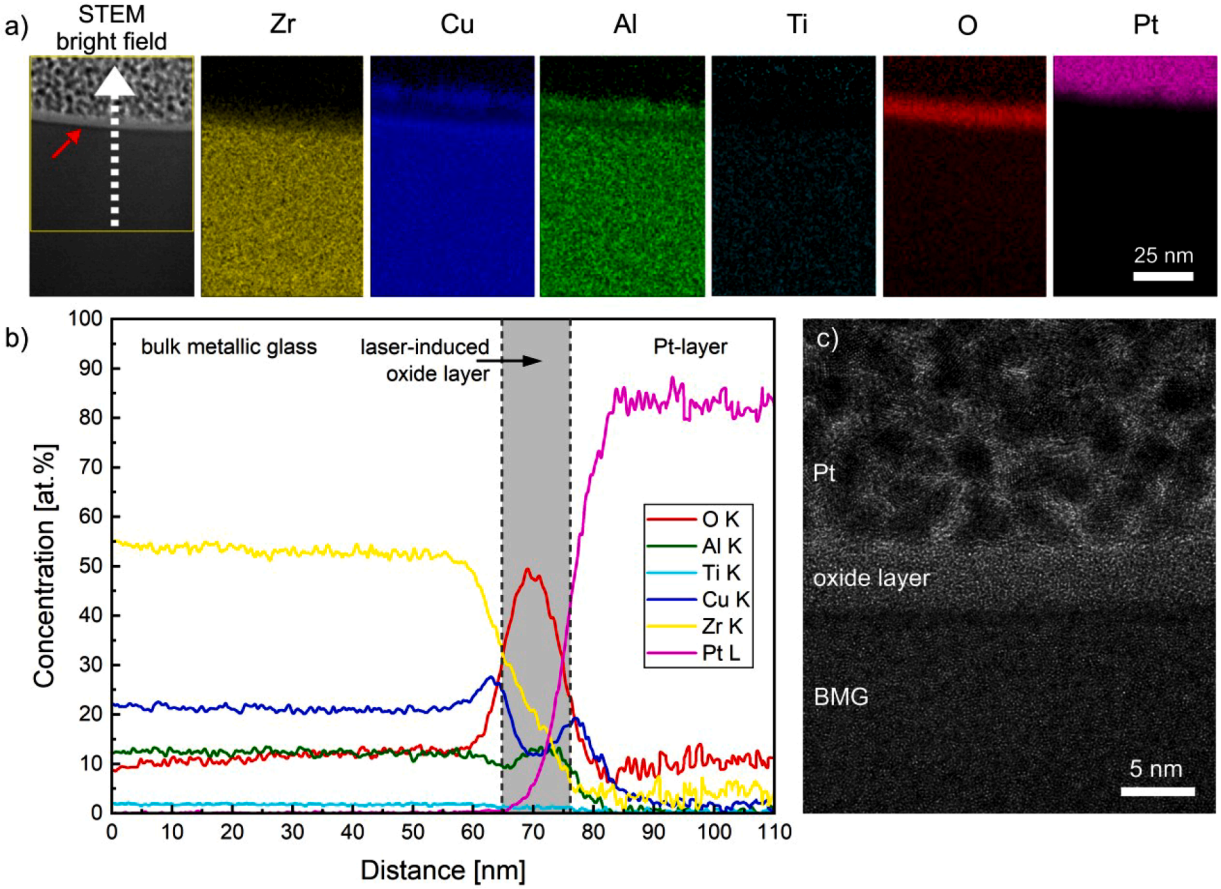

Fig. 8. Concentration profile of a cross-section prepared by focused ion beam from the LIPSS-covered $Zr_{61}Cu_{25}Al_{12}Ti_2$ surface irradiated at $F_0 = 0.7$ J/cm^2: (a) STEM EDXS maps of the involved elements, (b) EDXS profile along the white arrow indicated in (a) calculated by accumulating the data of the EDXS map in the yellow frame, and (c) high-resolution TEM bright field micrograph of the region between bulk material, oxide layer and the surface protecting Pt-layer.

4. Conclusions

Highly regular, well-pronounced LIPSS can be produced on the surface of Zr-based BMGs by fs-laser irradiation. Despite the different chemical compositions, the investigated BMGs exhibit very similar LIPSS periods, which can be described with the available SPP theories. While $Zr_{61}Cu_{25}Al_{12}Ti_2$, Vit105 and Vit106 revealed no laser-induced crystallization upon fs-laser irradiation, $Zr_{46}Cu_{46}Al_8$ showed a moderate transformation from the amorphous to the crystalline state within the sub-surface region. XPS analysis confirmed the presence of a native oxide layer on all pristine BMGs. Femtosecond laser irradiation leads to the formation of a laser-induced oxide layer of larger thickness consisting of an amorphous ZrCuAl-oxide. The obtained results provide an essential basis for the generation of BMG surfaces with tailored functional properties, which might enable novel tribological, optical, and biomedical applications.

Funding

The TEM and FIB facilities were established with a grant from the German Research Council (DFG) under project number 390918228 and 134573208, respectively.

CRediT authorship contribution statement

M. Wolff: Investigation, Formal analysis, Writing – original draft, Writing – review & editing, Visualization. **R. Wonneberger:** Conceptualization, Investigation, Formal analysis, Writing – original draft, Writing – review & editing, Visualization. **K.E. Freiberg:** Investigation, Formal analysis, Writing – original draft, Writing – review & editing, Visualization. **A. Hertwig:** Investigation, Formal analysis, Resources, Writing – original draft, Writing – review & editing, Visualization. **J. Bonse:** Investigation, Formal analysis, Writing – original draft, Writing – review & editing, Visualization. **L. Giebeler:** Investigation, Formal analysis, Writing – original draft, Writing – review & editing, Visualization. **A. Koitzsch:** Investigation, Formal analysis, Writing – original draft, Writing – review & editing, Visualization. **C. Kunz:** Investigation, Formal analysis, Writing – original draft, Writing – review & editing, Visualization. **H. Weber:** Investigation, Formal analysis, Writing – original draft, Writing – review & editing, Visualization. **J.K. Hufenbach:** Writing – original draft, Writing – review & editing. **F.A. Müller:** Conceptualization, Investigation, Resources, Writing – original draft, Writing – review & editing, Supervision. **S. Gräf:** Conceptualization, Investigation, Formal analysis, Writing – original draft, Writing – review & editing, Supervision.

Declaration of Competing Interest

The authors declare that they have no known competing financial interests or personal relationships that could have appeared to influence the work reported in this paper.

Data availability

Data will be made available on request.

Acknowledgements

Gundula Hidde from BAM (Division 6.1) is gratefully acknowledged for support with the ellipsometric measurements. Furthermore, we would like to thank Birgit Bartusch, Birgit Opitz and Sven Donath from IFW Dresden for support with sample preparation and thermomechanical as well as X-ray analysis. Julian Picker from FSU Jena is gratefully acknowledged for support and discussion with the XPS measurements.

References

[1] M.F. Ashby, A.L. Greer, Metallic glasses as structural materials, Scripta Mater. 54 (2006) 321–326.
[2] M. Miller, P. Liaw, Bulk Metallic Glasses, Springer Science, New York, 2008.
[3] P. Meagher, E.D. O'Cearbhaill, J.H. Byrne, D.J. Browne, Bulk metallic glasses for implantable medical devices and surgical tools, Adv. Mater. 28 (2016) 5755–5762.
[4] S. Mukherjee, J. Schroers, Z. Zhou, W.L. Johnson, W.K. Rhim, Viscosity and specific volume of bulk metallic glass-forming alloys and their correlation with glass forming ability, Acta Mater. 52 (2004) 3689–3695.
[5] V. Pacheco, D. Karlsson, J.J. Marattukalam, M. Stolpe, B. Hjorvarsson, U. Jansson, M. Sahlberg, Thermal stability and crystallization of a Zr-based metallic glass produced by suction casting and selective laser melting, J. Alloys Compd. 825 (2020), 153995.
[6] J. Antonowicz, P. Zalden, K. Sokolowski-Tinten, K. Georgarakis, R. Minikayev, A. Pietnoczka, F. Bertram, M. Chaika, M. Chojnacki, P. Dluzewski, K. Fronc, A. L. Greer, C. Jastrznbski, D. Klinger, C. Lemke, O.M. Magnussen, B. Murphy, K. Perumal, U. Ruett, K.J. Warias, R. Sobierajski, Devitrification of thin film Cu-Zr metallic glass via ultrashort pulsed laser annealing, J. Alloys Compd. 887 (2021), 161437.
[7] Y.F. Qian, M.Q. Jiang, Z.Y. Zhang, H. Huang, J. Hong, J.W. Yan, Microstructures and mechanical properties of Zr-based metallic glass ablated by nanosecond pulsed laser in various gas atmospheres, J. Alloys Compd. 901 (2022), 163717.
[8] L. Deng, A. Gebert, L. Zhang, H.Y. Chen, D.D. Gu, U. Kühn, M. Zimmermann, K. Kosiba, S. Pauly, Mechanical performance and corrosion behaviour of Zr-based bulk metallic glass produced by selective laser melting, Mater. Des. 189 (2020), 108532.
[9] Q. Gao, D. Ouyang, X.T. Liu, S.X. Wu, X. Huang, N. Li, Fabricating colorful bulk metallic glass surfaces by femtosecond laser processing, Mater. Chem. Phys. 266 (2021), 124561.
[10] J. Schroers, T. Nguyen, S. O'Keeffe, A. Desai, Thermoplastic forming of bulk metallic glass - Applications for MEMS and microstructure fabrication, Mater. Sci. Eng. A 449 (2007) 898–902.
[11] B. Sarac, J. Eckert, Thermoplasticity of metallic glasses: processing and applications, Prog. Mater Sci. 127 (2022), 100941.
[12] P. Hervier, Surface Functionalization of Zirconium Based Metallic Glasses, 2017, p. 218. PhD Thesis, Lisbonne.
[13] K. Sugioka, M. Meunier, A. Piqué, Laser Precision Microfabrication, Springer, Berlin, 2010.
[14] J. Bonse, S. Höhm, S.V. Kirner, A. Rosenfeld, J. Krüger, Laser-induced periodic surface structures - a scientific evergreen, IEEE J. Select. Top. Quant. Electron. 23 (2017), 9000615.
[15] F. Müller, C. Kunz, S. Gräf, Bio-inspired functional surfaces based on laser-induced periodic surface structures, Materials 9 (2016) 476.
[16] E. Stratakis, J. Bonse, J. Heitz, J. Siegel, G.D. Tsibidis, E. Skoulas, A. Papadopoulos, A. Mimidis, A.C. Joel, P. Comanns, J. Krüger, C. Florian, Y. Fuentes-Edfuf, J. Solis, W. Baumgartner, Laser engineering of biomimetic surfaces, Mater. Sci. Eng. R 141 (2020), 100562.
[17] J. Bonse, S. Gräf, Maxwell meets Marangoni-A review of theories on laser-induced periodic surface structures, Laser Photon. Rev. 14 (2020), 2000215.
[18] E. Allahyari, J.J.J. Nivas, S.L. Oscurato, M. Salvatore, G. Ausanio, A. Vecchione, R. Fittipaldi, P. Maddalena, R. Bruzzese, S. Amoruso, Laser surface texturing of copper and variation of the wetting response with the laser pulse fluence, Appl. Surf. Sci. 470 (2019) 817–824.
[19] J. Bonse, J. Krüger, S. Höhm, A. Rosenfeld, Femtosecond laser-induced periodic surface structures, J. Laser. Appl. 24 (2012), 042006.
[20] S. Gräf, F.A. Müller, Polarisation-dependent generation of fs-laser induced periodic surface structures, Appl. Surf. Sci. 331 (2015) 150–155.
[21] S. Gräf, C. Kunz, A. Undisz, R. Wonneberger, M. Rettenmayr, F.A. Müller, Mechano-responsive colour change of laser-induced periodic surface structures, Appl. Surf. Sci. 471 (2019) 645–651.
[22] L.T. Cangueiro, A.J. Cavaleiro, J. Morgiel, R. Vilar, Mechanisms of the formation of low spatial frequency LIPSS on Ni/Ti reactive multilayers, J. Phys. D 49 (2016), 365103.
[23] C. Florian, R. Wonneberger, A. Undisz, S.V. Kirner, K. Wasmuth, D. Spaltmann, J. Krüger, J. Bonse, Chemical effects during the formation of various types of femtosecond laser-generated surface structures on titanium alloy, Appl. Phys. A 126 (2020) 266.
[24] C. Kunz, J. Bonse, D. Spaltmann, C. Neumann, A. Turchanin, J.F. Bartolome, F. A. Müller, S. Gräf, Tribological performance of metal-reinforced ceramic composites selectively structured with femtosecond laser-induced periodic surface structures, Appl. Surf. Sci. 499 (2020), 143917.
[25] R. Wonneberger, W. Wisniewski, S. Lippmann, F.A. Müller, S. Gräf, A. Undisz, Surface amorphization of bulk NiTi induced by laser radiation, Surf. Interfaces 38 (2023), 102827.
[26] C.Z. Du, C.Y. Wang, T. Zhang, L.J. Zheng, Antibacterial performance of Zr-BMG, stainless steel, and titanium alloy with laser-induced periodic surface structures, ACS Appl. Bio Mater. 5 (2022) 272–284.
[27] H.X. Huang, P.L. Zhang, Z.S. Yu, L. Shen, H.C. Shi, Y.T. Tian, Femtosecond laser-induced transformation mechanism from 1D groove structure to 2D microholes structure on the surface of Zr-based metallic glasses, Opt. Laser Technol. 146 (2022), 107555.
[28] X.L. Wang, P.X. Lu, N.L. Dai, Y.H. Li, C.R. Liao, Y.X. Chang, G. Yang, Q.G. Zheng, Morphology and oxidation of Zr-based amorphous alloy ablated by femtosecond laser pulses, Appl. Phys. A 89 (2007) 547–552.

[29] C. Dold, M. Kachel, D. Wortmann, V. Wessels, A. Dohrn, A. Bruinink, F. Pude, J. Loeffler, R. Poprawe, K. Wegener, Surface structuring of zirconium-based bulk metallic glasses using ultrashort laser pulses, SPIE LASE 8967 (2014).

[30] D.V. Louzguine-Luzgin, C.L. Chen, L.Y. Lin, Z.C. Wang, S.V. Ketov, M.J. Miyama, A. S. Trifonov, A.V. Lubenchenko, Y. Ikuhara, Bulk metallic glassy surface native oxide: its atomic structure, growth rate and electrical properties, Acta Mater. 97 (2015) 282–290.

[31] S. Barlemont, P. Laffont, R. Daudin, A. Lenain, G. Colas, P.H. Cornuault, Strong dependency of the tribological behavior of CuZr-based bulk metallic glasses on relative humidity in ambient air, Friction 11 (2023) 785–800.

[32] K. Sun, R. Fu, X.W. Liu, L.M. Xu, G. Wang, S.Y. Chen, Q.J. Zhai, S. Pauly, Osteogenesis and angiogenesis of a bulk metallic glass for biomedical implants, Bioact. Mater. 8 (2022) 253–266.

[33] B. Sarac, L. Zhang, K. Kosiba, S. Pauly, M. Stoica, J. Eckert, Towards the better: intrinsic property amelioration in bulk metallic glasses, Sci. Rep. 6 (2016) 27271.

[34] R.M. Srivastava, J. Eckert, W. Loser, B.K. Dhindaw, L. Schultz, Cooling rate evaluation for bulk amorphous alloys from eutectic microstructures in casting processes, Mater. Trans. 43 (2002) 1670–1675.

[35] A. Gebert, D. Geissler, S. Pilz, M. Uhlemann, F.A. Davani, S. Hilke, H. Rosner, G. Wilde, Studies on stress corrosion cracking of Vit 105 bulk metallic glass, Front. Mater. 7 (2020) 128.

[36] H. Fujiwara, Spectroscopic Ellipsometry: Principles and Applications, Wiley, Tokyo, 2007.

[37] B. Johs, J.S. Hale, Dielectric function representation by B-splines, Phys. Stat. Solidi A 205 (2008) 715–719.

[38] C.L. Qin, W.M. Zhao, A. Inoue, Glass formation, chemical properties and surface analysis of Cu-based bulk metallic glasses, Int. J. Mol. Sci. 12 (2011) 2275–2293.

[39] J.M. Liu, Simple technique for measurements of pulsed Gaussian beam spot sizes, Opt. Lett. 7 (1982) 196–198.

[40] J. Bonse, S. Gräf, Ten open questions about laser-induced periodic surface structures, Nanomaterials 11 (2021) 3326.

[41] M.R. Querry, Optical Constants of Minerals and other Materials from the Millimeter to the Ultraviolet, 1987. Contractor Report CRDEC-CR-88009.

[42] M.A. Ordal, R.J. Bell, R.W. Alexander, L.L. Long, M.R. Querry, Optical properties of fourteen metals in the infrared and far infrared: Al, Co, Cu, Au, Fe, Pb, Mo, Ni, Pd, Pt, Ag, Ti, V, and W, Appl. Opt. 24 (1985) 4493–4499.

[43] M.A. Ordal, R.J. Bell, R.W. Alexander, L.A. Newquist, M.R. Querry, Optical properties of Al, Fe, Ti, Ta, W, and Mo at submillimeter wavelengths, Appl. Opt. 27 (1988) 1203–1208.

[44] O. Pena-Rodriguez, M. Caro, A. Rivera, J. Olivares, J.M. Perlado, A. Caro, Optical properties of Au-Ag alloys: an ellipsometric study, Opt. Mater. Express 4 (2014) 403–410.

[45] L. McMillon-Brown, P. Bordeenithikasem, F. Pinnock, J. Ketkaew, A.C. Martin, J. Schroers, A.D. Taylor, Measured optical constants of $Pd_{77.5}Cu_6Si_{16.5}$ bulk metallic glass, Opt. Mater. X1 (2019), 100012.

[46] D. Shauyenova, S. Jung, H. Yang, H. Yim, H. Ju, Electrical and optical properties of $Co_{75}Si_{15}B_{10}$ metallic glass nanometric thin films, Materials 14 (2021) 162.

[47] A. Gebert, P.F. Gostin, L. Schultz, Effect of surface finishing of a Zr-based bulk metallic glass on its corrosion behaviour, Corros. Sci. 52 (2010) 1711–1720.

[48] J.J.J. Nivas, S. Amoruso, Generation of supra-wavelength grooves in femtosecond laser surface structuring of silicon, Nanomaterials 11 (2021) 174.

[49] F. Dausinger, Strahlwerkzeug Laser: Energieeinkopplung und Prozesseffektivität, University of Stuttgart, Stuttgart, 1995, p. 143. Habilitation.

[50] S. Gräf, C. Kunz, S. Engel, T.J.Y. Derrien, F.A. Müller, Femtosecond laser-induced periodic surface structures on fused silica: the impact of the initial substrate temperature, Materials 11 (2018) 1340.

[51] S. Gräf, C. Kunz, F.A. Müller, Formation and properties of laser-induced periodic surface structures on different glasses, Materials 10 (2017) 933.

[52] J. Bonse, S.V. Kirner, J. Krüger, Laser-induced periodic surface structures (LIPSS), in: K. Sugioka (Ed.), Handbook of Laser Micro- and Nano-Engineering, Springer, Cham, 2021, pp. 879–936.

[53] M. Huang, F.L. Zhao, Y. Cheng, N.S. Xu, Z.Z. Xu, Origin of laser-induced near-subwavelength ripples: interference between surface plasmons and incident laser, ACS Nano 3 (2009) 4062–4070.

[54] J. Bonse, A. Rosenfeld, J. Krüger, On the role of surface plasmon polaritons in the formation of laser-induced periodic surface structures upon irradiation of silicon by femtosecond-laser pulses, J. Appl. Phys. 106 (2009), 104910.

[55] I. Gnilitskyi, T.J.Y. Derrien, Y. Levy, N.M. Bulgakova, T. Mocek, L. Orazi, High-speed manufacturing of highly regular femtosecond laser-induced periodic surface structures: physical origin of regularity, Sci. Rep. 7 (2017) 8485.

[56] X. Ji, Y. Shan, C. Ji, H. Wang, Z. Zhao, Slurry erosion behavior of two Zr-based bulk metallic glasses, Wear 476 (2021), 203684.

[57] H. Bo, J. Wang, S. Jin, H.Y. Qi, X.L. Yuan, L.B. Lin, Z.P. Jin, Thermodynamic analysis of the Al-Cu-Zr bulk metallic glass system, Intermetallics 18 (2010) 2322–2327.

[58] P.K. Liaw, G. Wang, J. Schneider, Bulk metallic glasses: overcoming the challenges to widespread applications, JOM 62 (2010) 69.

[59] Q. He, J. Xu, Locating malleable bulk metallic glasses in Zr-Ti-Cu-Al alloys with calorimetric glass transition temperature as an indicator, J. Mater. Sci. Technol. 28 (2012) 1109–1122.

[60] A.V. Naumkin, A. Kraut-Vass, S.W. Gaarenstroom, C.J. Powell, NIST X-Ray Photoelectron Spectroscopy Database, 2012.

[61] J. Heinrich, R. Busch, F. Müller, S. Grandthyll, S. Hüfner, Role of aluminum as an oxygen-scavenger in zirconium based bulk metallic glasses, Appl. Phys. Lett. 100 (2012), 071909.

[62] A. Samanta, Q.H. Wang, S.K. Shaw, H.T. Ding, Roles of chemistry modification for laser textured metal alloys to achieve extreme surface wetting behaviors, Mater. Des. 192 (2020), 108744.

[63] A.M. Kietzig, S.G. Hatzikiriakos, P. Englezos, Patterned superhydrophobic metallic surfaces, Langmuir 25 (2009) 4821–4827.

[64] J.Y. Long, M.L. Zhong, H.J. Zhang, P.X. Fan, Superhydrophilicity to superhydrophobicity transition of picosecond laser microstructured aluminum in ambient air, J. Colloid Interface Sci. 441 (2015) 1–9.

[65] M. Kilo, M. Hund, G. Sauer, A. Baiker, A. Wokaun, Reaction induced surface segregation in amorphous CuZr, NiZr and PdZr alloys - an XPS and SIMS depth profiling study, J. Alloys Compd. 236 (1996) 137–150.

[66] S.Y. Kwon, I.H. Jung, Thermodynamic assessment of the Al_2O_3-ZrO_2, CaO-Al_2O_3-ZrO_2, and Al_2O_3-SiO_2-ZrO_2 systems, Ceram. Int. 48 (2022) 5413–5427.

[67] V. Sawyer, X. Tao, H. Dong, B. Dashtbozorg, X.Y. Li, R. Sammons, H.S. Dong, Improving the tribological properties and biocompatibility of Zr-based bulk metallic glass for potential biomedical applications, Materials 13 (2020) 1960.

[68] W. Kai, Y.R. Chen, T.H. Ho, H.H. Hsieh, D.C. Qiao, F. Jiang, G. Fan, P.K. Liaw, Air oxidation of a $Zr_{58}Cu_{22}Al_{12}Fe_8$ bulk metallic glass at 350-550°C, J. Alloys Compd. 483 (2009) 519–525.